RSC Advances

PAPER

View Article Online
View Journal | View Issue

Open Access Article. Published on 06 April 2022. Downloaded on 10/28/2025 6:47:30 AM.
This article is licensed under a Creative Commons Attribution-NonCommercial 3.0 Unported Licence.

Check for updates

Cite this: *RSC Adv.*, 2022, **12**, 10592

$SrTiO_3$@NiFe LDH core–shell composites for photocatalytic CO_2 conversion†

Lian Zhu[a] and Zhengping Qiao *[b]

Received 22nd February 2022
Accepted 29th March 2022

DOI: 10.1039/d2ra01178f

rsc.li/rsc-advances

A series of core@shell $SrTiO_3$@NiFe LDH composites (STONFs) were synthesized and their photocatalytic CO_2 reduction performance was studied. The photocatalyst STONF **2** exhibited enhanced CO_2 reduction performance with CO yield of 7.9 μmol g^{-1} h^{-1}. The yield was 25.7 times and 8.8 times higher than that of NiFe LDH and $SrTiO_3$ respectively, and also higher than most LDH based photocatalysts. Compared with two individual components, STONFs exhibited their combined merits of widened absorption spectrum, higher transportation efficiency and alleviated recombination of e^-/h^+ pairs. In addition, there were fewer oxygen vacancies in STONF **2** than as-prepared $SrTiO_3$. Lower oxygen vacancies concentration would increase the opportunity of direct bonding between interface atoms of two components and successively increase the electron transportation and separation. These factors synergistically contributed to enhanced photocatalytic performance. This work will provide new insight for designing complementary multi-component photocatalysis systems.

1. Introduction

Global warming caused by emission of greenhouse gas, especially CO_2, has attracted increasing concern. Light-driven CO_2 conversion into value-added chemicals is one of the attractive ways to mitigate the situation. To date, great efforts had been made to develop a photocatalytic CO_2 conversion system.[1–6] However, there still are two factors impeding photocatalytic performance enhancement.[7,8] On the one hand, some photocatalysts absorb light in a narrow spectrum and can't efficiently utilize solar energy to generate sufficient carriers (e^-/h^+ pairs). On the other hand, e^-/h^+ pairs recombine severely inside or on the surface of catalysts. Constructing composites photocatalysts is a feasible way, in which merits of complementary components are combined. Components play different roles in the photocatalysis system and exhibit overall advantages. Well-matched energy band structure in composites can facilitate carrier separation. In addition, tight combination between components can alleviate carrier recombination in transportation process.[9–12]

NiFe layered double hydroxide (NiFe LDH) is brucite-like layers with a fraction of octahedrally coordinated Ni^{2+} and Fe^{3+}. It has gained attention in photocatalysis because of low price, environmental friendliness, post-catalysis recovery, and wide absorption spectrum. However, LDH-based photocatalysts possess high recombination rate of e^-/h^+ pairs and high charge transfer resistance, which leads to low CO_2 reduction efficiency and restricts its practical application.[13,14]

The problem can be mitigated by integrating NiFe LDH with other substance. Strontium titanate ($SrTiO_3$), a typical perovskite type semiconductor, is a competitive candidate because of its low price, components abundance, structural stability, and environmental friendliness. Specifically, $SrTiO_3$ possesses low charge transfer resistance and high crystallinity, which leads to high transportation efficiency and limited recombination of e^-/h^+ pairs at defects.[15–17]

Herein, $SrTiO_3$@NiFe LDH core–shell composites (STONFs) were synthesized, and their photocatalytic CO_2 reduction performance was studied. The photocatalyst STONF **2** exhibited enhanced CO_2 reduction performance with CO yield of 7.9 μmol g^{-1} h^{-1}. The yield was 25.7 times and 8.8 times higher than that of NiFe LDH and $SrTiO_3$ respectively, and also higher than most LDH based photocatalysts. Compared with two individual components, STONFs exhibited their combined merits of widened absorption spectrum, higher transportation efficiency and alleviated recombination of e^-/h^+ pairs. NiFe LDH shell served as light absorbent and generated e^-/h^+ pairs. Then electrons transferred onto the $SrTiO_3$ core for CO_2 reduction because of matched band structure. In addition, there were fewer oxygen vacancies in STONFs than as-prepared $SrTiO_3$. Lower oxygen vacancies concentration would increase the opportunity of direct bonding between interface atoms of two components and successively increase the electron transportation and separation. These factors synergistically contributed to enhanced photocatalytic performance. This work will

[a]School of Chemistry, Sun Yat-Sen University, Guangzhou, China

[b]School of Materials Science and Engineering, Sun Yat-Sen University, Guangzhou, China. E-mail: cesqzp@mail.sysu.edu.cn

† Electronic supplementary information (ESI) available: TEM, SEM and element mappings of STONFs, characterization of 5-cycle post-catalysis STONF **2**, CO_2 reduction performance of other photocatalysts, transient PL decays fitting parameters and XPS survey spectrum. See DOI: 10.1039/d2ra01178f

© 2022 The Author(s). Published by the Royal Society of Chemistry

Open Access Article. Published on 06 April 2022. Downloaded on 10/28/2025 6:47:30 AM.
This article is licensed under a Creative Commons Attribution-NonCommercial 3.0 Unported Licence.

provide new insight for designing complementary multi-component photocatalysis system.

2. Experimental

All the reagents were purchased commercially and used without further purification.

2.1 Synthesis of $SrTiO_3$

$SrTiO_3$ was synthesized under microwave irradiation, which consumes much shorter time (14 min) than that reported in literatures (48 h).[18,19] The process is shown as followed. In ice-water bath, 750 μL $TiCl_4$ and 3 mL 1,2-propanediol were added into 75 mL H_2O, following by 5 min stirring. Then 90 mL 3 mol L^{-1} LiOH aqueous was added, following by 30 min stirring. After that, 30 mL 0.24 mol L^{-1} $SrCl_2$ aqueous was added, following by 30 min stirring. Then the mixture was irradiated under 250 W microwave for 14 min. The participate was washed by 1.5 wt% acetic acid aqueous for 3 times and dried at 60 °C for 8 h.

2.2 Synthesis of $SrTiO_3$@NiFe LDH

Add certain amount of $SrTiO_3$ and 18 g urea into 100 mL 0.025 mol L^{-1} $Ni(NO_3)_2$ and 0.008 mol L^{-1} $Fe(NO_3)_3$ mixture. After 30 min ultrasonication, the mixture was transferred into autoclave for 6 h hydrothermal reaction at 100 °C. The participate was washed by acetic acid aqueous (15 mL 0.5 wt%, 3 times) and water–ethanol ($V_w : V_e = 1 : 1$, once) consequently, and then was dried at 60 °C for 8 h. The products were named as STONF **1**, **2** and **3**, when $SrTiO_3$ amount was 0.1542 g, 0.4586 g, 1.3762 g respectively.

2.3 Photocatalysis experiment

5 mg photocatalyst was added into 4 mL acetonitrile and 1 mL triethanolamine, following by 10 min ultrasonication. Then pure CO_2 was continuously pumped into the mixture for 20 min to remove air. This mixture was exposed under visible light and stirred vigorously. The light source was a 300 W Xe lamp with a 420 nm cut-off filter. Light intensity was 120 mW cm^{-2}. After illumination for 3 h, the produced gases were analysed and quantified by gas chromatography.

2.4 Material characterization

Powder X-ray diffraction (XRD) analysis was performed using a Rigaku Dmax-2000 diffractometer equipped with Cu Kα (λ = 0.15406 nm) radiation. Inductively coupled plasma spectrometry (ICP, Cary5000) was used for multi-elemental analyses. Catalyst morphologies were observed with transmission electron microscopy (TEM, JEOL JEM-2100F 200 kV) and SEM (Zeiss Gemini SEM 500). UV-visible absorption (UV-vis ABS) was conducted on a PerkinElmer UV-vis-NIR Spectrophotometer Lambda 950 at room temperature. Time resolved photoluminescence spectra were conducted by Edinburgh FLS920 equipped with a picosecond pulsed light emitting diode (Edinburgh EPLED-360). The excitation and emission wavelength were 360 nm and 430 nm, respectively. Photocurrent density, Nyquist plots, and Mott–Schottky plot measurements were obtained using CHI 760D electrochemical workstations (CHI, Shanghai). The electrolyte is 0.1 mol L^{-1} Na_2SO_4 aqueous solution. The auxiliary electrode is Pt wire. Generated gas was tested and analysed using a gas chromatograph equipped with FID (GC 9790 II) and nitrogen acted as the carrier gas. X-ray photoelectron spectroscopy (XPS) was conducted on ESCALAB 250, Thermo Fisher Scientific. Electron Paramagnetic Resonance (EPR) was conducted on Bruker A300 under 77 K. Microwave frequency was 8 GHz, modulation amplitude was 8G, microwave power was 1.00 mW, and modulation frequency was 100 kHz. ^{1}H NMR were carried on 400 MHz Bruker Advance III at room temperature. Magnetic field intensity was 9.4 T.

3. Results and discussion

As described in the experimental section, a series of $SrTiO_3$@NiFe LDH composites (STONFs) with different molar ratios were synthesized. The molar ratios of $SrTiO_3$ to NiFe LDH of the composites were characterized by ICP-AES, which was 1 : 0.6, 1 : 1.3, 1 : 5.4 for STONF **1**, **2** and **3**, respectively. PXRD patterns of the as-prepared samples are shown in Fig. 1a. All of diffraction peaks can be indexed as $SrTiO_3$ (PDF# 86-0178) and NiFe LDH (PDF# 40-0215, shown by arrows). The widen diffraction peaks of NiFe LDH showed its nanocrystal size.

Morphology of samples was investigated by TEM, SEM and EDS element mappings. As-prepared angular $SrTiO_3$ (Fig. 1b) became spherical after growth of NiFe LDH (Fig. 1c and d), indicating $SrTiO_3$ crystals were nano-scaled dissolving under alkaline NiFe LDH preparation system. Another difference STONFs from $SrTiO_3$ was that there were nanoparticles growing on $SrTiO_3$ core. EDS element mappings of STONFs (Fig. 1e–j and S1†) showed the existence of Sr, Ti, Ni and Fe belonging to $SrTiO_3$ and NiFe LDH. With the increasing of content, the NiFe LDH incompletely coated (Fig. S1a and b†), homogeneously

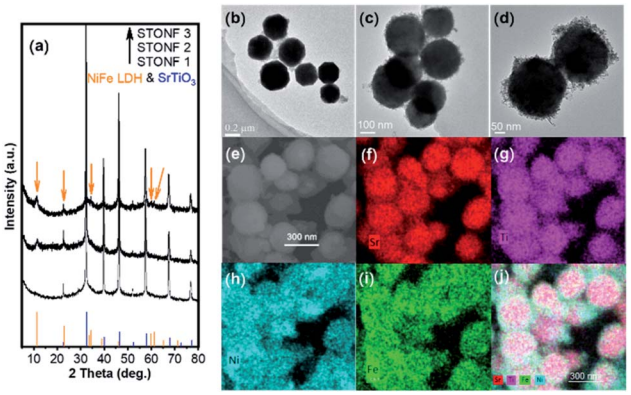

Fig. 1 (a) PXRD pattern of as-prepared catalysts (orange arrows show the peaks of NiFe LDH); (b) TEM image of as-prepared $SrTiO_3$; (c and d) TEM images of STONF **2**; (e) SEM image of STONF **2**; (f–i) EDS element mappings of selected area; (j) overlapping image of (e–i).

Open Access Article. Published on 06 April 2022. Downloaded on 10/28/2025 6:47:30 AM.
This article is licensed under a Creative Commons Attribution-NonCommercial 3.0 Unported Licence.

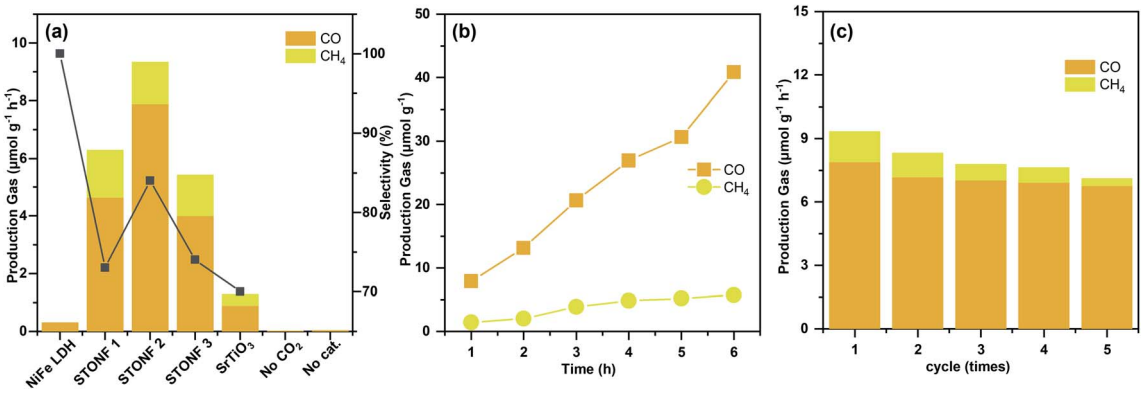

Fig. 2 (a) Production gas amount and corresponding CO selectivity of as-prepared catalysts; (b) time-dependent production gas amount of STONF **2**; (c) recycling test of STONF **2** for 5 times with CO_2 refilled every 3 h.

coated (Fig. 1c and d) on $SrTiO_3$ for STONF **1** and **2**, respectively. The NiFe LDH became self-aggregated for STONF **3**.

Photocatalytic CO_2 reduction experiments were carried out under visible light irradiation ($\lambda > 420$ nm), and the results were summarized in Fig. 2a–c. As predicted by morphology, STONF **2** was completely core–shell structure, showed the highest CO yield (7.9 μmol g^{-1} h^{-1}) and selectivity (84%). As showed in Fig. S2,† no liquid reduction products were detected. The CO yield was 1.7, 2.0, 25.7 and 8.8 times higher than that of STONF **1** (4.6 μmol g^{-1} h^{-1}), STONF **3** (4.0 μmol g^{-1} h^{-1}), as-prepared NiFe LDH (0.3 μmol g^{-1} h^{-1}) and $SrTiO_3$ (0.8 μmol g^{-1} h^{-1}), respectively. As shown in Fig. S3,† $SrTiO_3$ showed weak visible light absorption due to surface defects, which was responsible for its visible photocatalysis.[20–24] The photocatalysis efficiency were roughly compared by CO yield. STONF **2** showed higher photocatalytic performance than reported CoAl LDH, MgAl LDH, ZnCr LDH, NiAl LDH, NiFe LDH, $SrTiO_3$ based photocatalysts,[25–38] as summarized in Table S1.†

In addition, blank contrast experiment was performed by using N_2 to replace CO_2, the catalyst was selected as STONF **2**. No CO or CH_4 were detected, which confirmed that CO and CH_4 was originated from CO_2.

The continuity and stability of STONF **2** were shown in Fig. 2b, c and S4.† From Fig. 2b, one can see the yields of CO and CH_4 increased almost linearly with irradiation time and exhibited ascending CO selectivity. Recycling catalytic system with refreshed CO_2 every 3 h for 5 times under continuous light irradiation was conducted to test the stability. From which one can see that the CO production kept stable (Fig. 2c). The morphology and phase composition (Fig. S4†) didn't change by comparation of that for STONF **2** before photocatalysis.

UV-vis absorption spectrum and transient photocurrent response measurement were conducted to study the photophysical properties (Fig. 3). STONFs showed visible light absorption. The photocurrent response (Fig. 3b) of STONFs was **2** > **1** > **3**, which was in accordance with their photocatalysis performance. STONF **2** exhibited the highest photocurrent response, indicating the highest light utilization efficiency and the most photo-generated carriers.

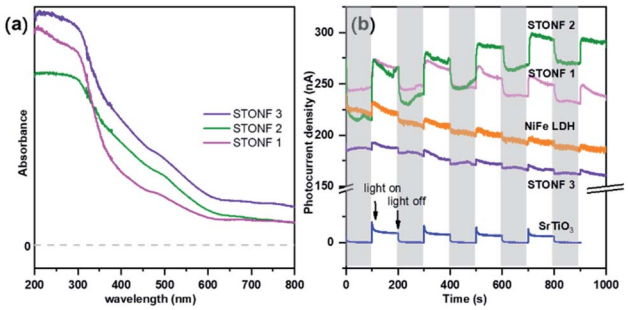

Fig. 3 (a) UV-vis absorption spectrum and (b) transient photocurrent response of as-prepared catalysts.

In order to shed light on the improved catalysis performance of STONFs, the band structures of as-prepared $SrTiO_3$ and NiFe LDH were examined. The Tauc plots (Fig. 4a) that calculated from plots in UV-vis absorption spectrum showed the energy gap (E_g) of $SrTiO_3$ and NiFe LDH were 3.1 eV and 2.2 eV, respectively. The flat band potentials (E_f) of $SrTiO_3$ and NiFe LDH obtained by Mott–Schottky measurements (Fig. 4b) were −0.75 V and −0.87 V (*vs.* NHE), respectively. Combining E_g and E_f, band structure of STONF composites and photocatalytic mechanism were showed in Fig. 4c. The detailed calculation method was shown in ESI.† Induced by visible light, electrons in NiFe LDH shell were excited to conduction band, and accordingly holes situated in valence band. Then electrons rapidly transferred to conduction band of $SrTiO_3$ core, and converted CO_2 to CO. Meanwhile, holes were consumed by triethanolamine (TEOA). The well-matched band structure facilitated carriers separation, which was desirable for photocatalysis.

The results were further confirmed by transient photoluminescence decays (Fig. 4d). The corresponding fitting parameters were listed in Table S2.† The lifetime of STONFs was 3.19 ns, 5.03 ns and 2.82 ns for **1**, **2** and **3**, respectively. STONF **2** showed the longest lifetime, suggesting the highest separation and transportation efficiency.

The results of electrochemical impedance spectroscopy (EIS) and corresponding fitted circuit model were shown in Fig. 4e.

 © 2022 The Author(s). Published by the Royal Society of Chemistry

Open Access Article. Published on 06 April 2022. Downloaded on 10/28/2025 6:47:30 AM.
This article is licensed under a Creative Commons Attribution-NonCommercial 3.0 Unported Licence.

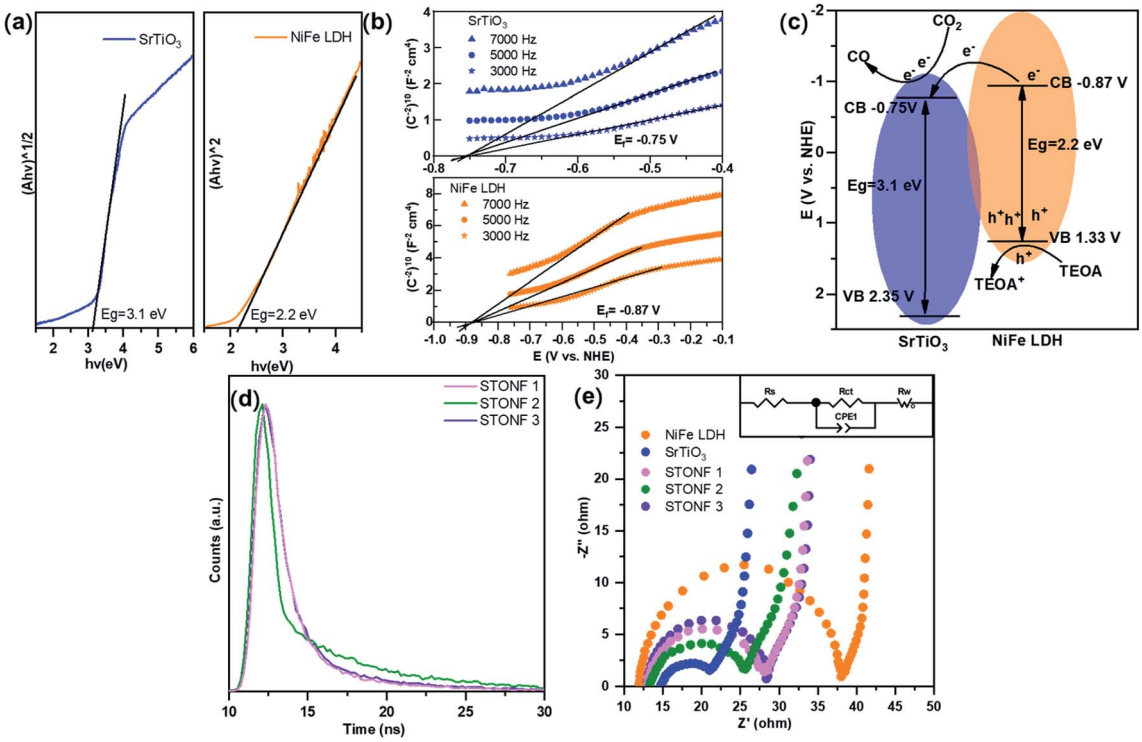

Fig. 4 (a) Tauc plots and (b) Mott–Schottky plots of $SrTiO_3$ and NiFe LDH; (c) schematic illustration of band structure alignment in STONFs composites; (d) transient PL decays and (e) Nyquist plots of as-prepared catalysts.

The impedance curves consisted one capacitive loop in high frequency region and one Warburg diffusion line in low frequency region. The capacitive loop was assigned to charge transfer resistance (R_{ct}) and this was related with photocatalysis. As shown in Table S3,† R_{ct} of $SrTiO_3$ (10.22 Ω cm^{-2}) was much smaller than that of NiFe LDH (25.40 Ω cm^{-2}), indicating $SrTiO_3$ was a good electron transporter. R_{ct} values were **2** < **1** < **3** (13.08 < 15.38 < 16.06 Ω cm^{-2}), which was in accordance with their photocatalytic performance.

Considering the results of EIS and transient PL decays, it was obvious that integrating components with matched band structure can promote carriers separation and transportation efficiency. Photoelectron produced by NiFe LDH shell transferred to $SrTiO_3$ core whose resistance was much lower than that of NiFe LDH. Therefore, the combination of e^-/h^+ pairs were prevented efficiently. $SrTiO_3$ has merit of stability and is cheaper than noble metal that commonly used in photocatalyst modification strategy. Among all the samples in our experiment, STONF **2** owned complete core shell structure and exhibited most efficient electron transformation.

As deduced from TEM (Fig. 1b–d), $SrTiO_3$ crystals were dissolved in nanoscale and thus the followed NiFe LDH growth was on the fresh crystal surface. It is well known that reducing interface defects, typically oxygen vacancies in oxide catalysts can decrease carriers recombination and thus increase the photocatalysis performance.[20,39,40] So, it is necessary to study the oxygen vacancies in STONF **2**. The ratio of Ti^{3+} and Ti^{4+} can reveal the oxygen vacancy contents. The reason was shown as follows. The lattice oxygen in $SrTiO_3$ was released to the gas phase due to the dissociation of Ti–O bond, usually the surface Ti–O bond, thus forming oxygen vacancies (V_O) and Ti^{3+}, as denoted in eqn (1) and (2).[15,41,42]

$$SrTiO_3 = SrTiO_{3-x} + \frac{1}{2}xO_2 + 2xe^- + xV_O \quad (1)$$

$$SrTiO_3 = SrTi(\text{IV})_{1-2x}\ Ti(\text{III})_{2x}\ O_{3-x} + \frac{1}{2}xO_2 + xV_O \quad (2)$$

So, X-ray photoelectron spectroscopy (XPS) was studied. The results were shown Fig. S5, S6,† 5a and b (high-resolution spectra for Ti 2p and O 1s). The peaks around 458.5 and 458.0 eV in the Ti $2p_{5/2}$ region are the characteristic signals of Ti^{4+} and Ti^{3+}.[43–45] The calculated relative Ti^{3+} species ratios were summarized in Table 1. The peak area ratio of Ti^{3+} and Ti^{4+} (R_1 value) in STONF **2** was 0.73, which was lower than that in $SrTiO_3$ (0.97), indicating less oxygen vacancies in STONF **2**. This probably was due to the $SrTiO_3$ crystals nano-scaled dissolution after NiFe LDH surface growth. The oxygen vacancy in the interface of $SrTiO_3$ and NiFe LDH was successively decreased. This would increase the opportunity of direct bonding between interface atoms of two components. The two components share the interface O atoms, so direct bonding was based on breaking down H–O bonds for NiFe hydroxide. O species in NiFe LDH attributed from M–O (M = Ni, Fe), H–O, and O of interlayer Ac^-.[46,47]

As summarized in Table 2, STONF **2** showed smaller ratio of H–O and M–O contents (R_2) (0.80) than bare NiFe LDH (1.08). This result indicated that the relative amount of H–O bonds

Open Access Article. Published on 06 April 2022. Downloaded on 10/28/2025 6:47:30 AM.
This article is licensed under a Creative Commons Attribution-NonCommercial 3.0 Unported Licence.

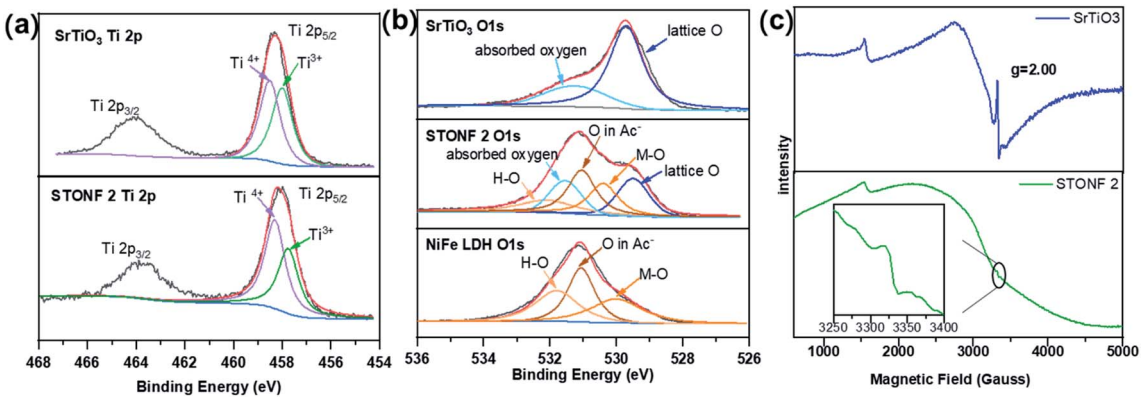

Fig. 5 XPS spectra of (a) the Ti 2p region and (b) O 1s region for as-prepared catalysts; (c) EPR signals of $SrTiO_3$ and STONF **2**.

Table 1 Chemical state of titanium species over $SrTiO_3$ and STONFs

	Ti^{4+}		Ti^{3+}		R_1
Catalyst	BE (eV)	Cont. (%)	BE (eV)	Cont. (%)	Cont. (Ti^{3+})/ Cont. (Ti^{4+})
$SrTiO_3$	458.51	50.8%	458.00	49.2%	0.97
STONF 1	458.33	53.0%	457.79	47.0%	0.89
STONF 2	458.30	57.7%	457.75	42.3%	0.73
STONF 3	458.34	53.3%	457.76	46.7%	0.88

Table 2 Chemical state of oxygen species over NiFe LDH and STONFs

	H–O		M–O		R_2
Catalyst	BE (eV)	Cont. (%)	BE (eV)	Cont. (%)	Cont. (H–O)/ Cont. (M–O)
NiFe LDH	531.79	32.9%	530.00	30.5%	1.08
STONF 1	532.04	23.9%	529.50	26.6%	0.88
STONF 2	532.09	25.6%	530.39	32.0%	0.80
STONF 3	532.10	14.62%	529.48	13.3%	1.09

decreased, which was consistency of deduction from Ti 2p analysis.[48–50]

In addition, X-band electron paramagnetic resonance spectroscopy (EPR) was also carried out to examine oxygen vacancies due to the existence of single electron in Ti^{3+}. The results were shown in Fig. 5c. The intense and sharp signal in $SrTiO_3$ and much weaker signal in STONF **2** at $g = 2.00$ indicated less oxygen vacancies in STONF **2**,[51–53] in accordance with the XPS results. Lower oxygen vacancies concentration would increase the opportunity of direct bonding between interface atoms of two components and successively increased the electron transportation and separation. This was probably one reason for the high catalysis performance of STONF **2**.

4. Conclusions

In summary, $SrTiO_3$@NiFe LDH core–shell composite was synthesized, and their photocatalytic CO_2 reduction performance was studied. The photocatalyst STONF **2** exhibited enhanced CO_2 reduction performance with CO yield of 7.9 μmol g^{-1} h^{-1}. The yield was 25.7 times and 8.8 times higher than that of as-prepared NiFe LDH and $SrTiO_3$ respectively, and also higher than most of LDH based photocatalysts. $SrTiO_3$ and NiFe LDH had matched band structure. NiFe LDH shell served as light absorbent and generated e^-/h^+ pairs. Then electrons transferred onto the $SrTiO_3$ core for CO_2 reduction. STONFs owned merits of both components. Widened absorption spectrum was beneficial for carriers generation. Smaller charge transfer resistance and longer carriers lifetime indicated higher carriers separation and transportation efficiency. The complete coating, fewer oxygen vacancies at interface and tight combination increased the charge transportation and thus decreased carries recombination. These factors synergistically contributed to enhanced photocatalytic performance. This work will provide new insight for designing complementary multi-component photocatalysis system.

Author contributions

Lian Zhu: conceptualization, investigation, methodology, project administration, visualization, writing – original draft. Zhengping Qiao: funding acquisition, resources, supervision, writing – review & editing.

Conflicts of interest

There are no conflicts to declare.

Acknowledgements

This work was supported by the National Natural Science Foundation of China (No. 21571193) and the Open Funds of the State Key Laboratory of Rare Earth Resources Utilization RERU2013012.

Notes and references

1 L. Bai, H. Huang, S. Yu, D. Zhang, H. Huang and Y. Zhang, *J. Energy Chem.*, 2022, **64**, 214–235.
2 C. I. Ezugwu, S. Liu, C. Li, S. Zhuiykov, S. Roy and F. Verpoort, *Coord. Chem. Rev.*, 2022, **450**, 214245.

 © 2022 The Author(s). Published by the Royal Society of Chemistry

Open Access Article. Published on 06 April 2022. Downloaded on 10/28/2025 6:47:30 AM.
This article is licensed under a Creative Commons Attribution-NonCommercial 3.0 Unported Licence.

3 M. Humayun, C. Wang and W. Luo, *Small Methods*, 2021, 2101395.
4 H.-J. Son, C. Pac and S. O. Kang, *Acc. Chem. Res.*, 2021, **54**, 4530–4544.
5 S. Singh, A. Modak, K. K. Pant, A. Sinhamahapatra and P. Biswas, *ACS Appl. Nano Mater.*, 2021, **4**, 8644–8667.
6 K. Ren, S. Yue, C. Li, Z. Fang, K. A. M. Gasem, J. Leszczynski, S. Qu, Z. Wang and M. Fan, *J. Mater. Chem. A*, 2022, **10**, 407–429.
7 Q. Wang and K. Domen, *Chem. Rev.*, 2020, **120**, 919–985.
8 A. Behera, A. K. Kar and R. Srivastava, *Mater. Horiz.*, 2022, **9**, 607–639.
9 V. Balakumar, S. Selvarajan, A. Baishnisha and S. Kathiresan, *Appl. Surf. Sci.*, 2022, **577**, 151924.
10 C.-J. Chang, J.-K. Chen, K.-S. Lin, C.-Y. Huang and C.-L. Huang, *Int. J. Hydrogen Energy*, 2021, **46**, 11357–11368.
11 H. Wu, X. Y. Kong, X. Wen, S.-P. Chai, E. C. Lovell, J. Tang and Y. H. Ng, *Angew. Chem., Int. Ed.*, 2021, **60**, 8455–8459.
12 Z. Zhan, H. Wang, Q. Huang, S. Li, X. Yi, Q. Tang, J. Wang and B. Tan, *Small*, 2022, **18**, 2105083.
13 K. Wang, T. Wang, Q. A. Islam and Y. Wu, *Chin. J. Catal.*, 2021, **42**, 1944–1975.
14 H. Boumeriame, E. S. Da Silva, A. S. Cherevan, T. Chafik, J. L. Faria and D. Eder, *J. Energy Chem.*, 2022, **64**, 406–431.
15 R. A. De Souza, *Curr. Opin. Solid State Mater. Sci.*, 2021, **25**, 100923.
16 T. Takata, J. Jiang, Y. Sakata, M. Nakabayashi, N. Shibata, V. Nandal, K. Seki, T. Hisatomi and K. Domen, *Nature*, 2020, **581**, 411–414.
17 T. Takata and K. Domen, *J. Phys. Chem. C*, 2009, **113**, 19386–19388.
18 L. Mu, Y. Zhao, A. Li, S. Wang, Z. Wang, J. Yang, Y. Wang, T. Liu, R. Chen, J. Zhu, F. Fan, R. Li and C. Li, *Energy Environ. Sci.*, 2016, **9**, 2463–2469.
19 L. Dong, H. Shi, K. Cheng, Q. Wang, W. Weng and W. Han, *Nano Res.*, 2014, **7**, 1311–1318.
20 H. Tan, Z. Zhao, W.-b. Zhu, E. N. Coker, B. Li, M. Zheng, W. Yu, H. Fan and Z. Sun, *ACS Appl. Mater. Interfaces*, 2014, **6**, 19184–19190.
21 U. Sulaeman, S. Yin and T. Sato, *Adv. Nanopart.*, 2013, **2**, 01–05.
22 H. Che, J. Chen, K. Huang, W. Hu, H. Hu, X. Liu, G. Che, C. Liu and W. Shi, *J. Alloys Compd.*, 2016, **688**, 882–890.
23 S.-F. Yang, C.-G. Niu, D.-W. Huang, H. Zhang, C. Liang and G.-M. Zeng, *Environ. Sci.: Nano*, 2017, **4**, 585–595.
24 L. Tong, L. Ren, A. Fu, D. Wang, L. Liu and J. Ye, *Chem. Commun.*, 2019, **55**, 12900–12903.
25 S. Shoji, G. Yin, M. Nishikawa, D. Atarashi, E. Sakai and M. Miyauchi, *Chem. Phys. Lett.*, 2016, **658**, 309–314.
26 S. Wang, K. Teramura, T. Hisatomi, K. Domen, H. Asakura, S. Hosokawa and T. Tanaka, *ACS Appl. Energy Mater.*, 2020, **3**, 1468–1475.
27 S. Wang, K. Teramura, T. Hisatomi, K. Domen, H. Asakura, S. Hosokawa and T. Tanaka, *ACS Sustainable Chem. Eng.*, 2021, **9**, 9327–9335.
28 K.-i. Katsumata, K. Sakai, K. Ikeda, G. Carja, N. Matsushita and K. Okada, *Mater. Lett.*, 2013, **107**, 138–140.
29 S. Kumar, L. J. Durndell, J. C. Manayil, M. A. Isaacs, C. M. A. Parlett, S. Karthikeyan, R. E. Douthwaite, B. Coulson, K. Wilson and A. F. Lee, *Part. Part. Syst. Charact.*, 2018, **35**, 1700317.
30 Y.-f. Miao, R.-t. Guo, J.-w. Gu, Y.-z. Liu, G.-l. Wu, C.-p. Duan and W.-g. Pan, *ACS Appl. Nano Mater.*, 2021, **4**, 4902–4911.
31 C. Ning, Z. Wang, S. Bai, L. Tan, H. Dong, Y. Xu, X. Hao, T. Shen, J. Zhao, P. Zhao, Z. Li, Y. Zhao and Y.-F. Song, *Chem. Eng. J.*, 2021, **412**, 128362.
32 S. Tonda, S. Kumar, M. Bhardwaj, P. Yadav and S. Ogale, *ACS Appl. Mater. Interfaces*, 2018, **10**, 2667–2678.
33 Y. Wu, Y. Gong, J. Liu, T. Chen, Q. Liu, Y. Zhu, L. Niu, C. Li, X. Liu, C. Q. Sun and S. Xu, *J. Alloys Compd.*, 2020, **831**, 154723.
34 J. Xu, X. Liu, Z. Zhou, L. Deng, L. Liu and M. Xu, *Energy Fuels*, 2021, **35**, 16134–16143.
35 J. Xu, X. Liu, Z. Zhou, L. Deng, L. Liu and M. Xu, *Energy Fuels*, 2021, **35**, 10820–10831.
36 S. Zhao, D. Pan, Q. Liang, M. Zhou, C. Yao, S. Xu and Z. Li, *J. Phys. Chem. C*, 2021, **125**, 10207–10218.
37 X. Zhao, X. Zhao, I. Ullah, L. Gao, J. Zhang and J. Lu, *Catal. Lett.*, 2021, **151**, 1683–1692.
38 S. Kumar, M. A. Isaacs, R. Trofimovaite, L. Durndell, C. M. A. Parlett, R. E. Douthwaite, B. Coulson, M. C. R. Cockett, K. Wilson and A. F. Lee, *Appl. Catal., B*, 2017, **209**, 394–404.
39 S. Jia, J. Gao, Q. Shen, J. Xue, Z. Zhang, X. Liu and H. Jia, *J. Mater. Sci.: Mater. Electron.*, 2021, **32**, 13369–13381.
40 Y. Ham, T. Hisatomi, Y. Goto, Y. Moriya, Y. Sakata, A. Yamakata, J. Kubota and K. Domen, *J. Mater. Chem. A*, 2016, **4**, 3027–3033.
41 C.-Y. Guo and X. Qi, *Mater. Des.*, 2019, **179**, 107888.
42 Z. Zhang, H. Yan, S. Wang, M. Wang, L. Ren, C. Chen and K. Jin, *J. Mater. Sci.*, 2019, **54**, 4780–4787.
43 R. Hong, C. Deng, M. Jing, H. Lin, C. Tao and D. Zhang, *Opt. Mater.*, 2019, **95**, 109224.
44 Y. Zhao, M. Zhang, W. Wang, W. Song, K. Jiang and X. Zhang, *J. Mater. Sci.: Mater. Electron.*, 2021, **32**, 22910–22920.
45 Y. Qin, F. Fang, Z. Xie, H. Lin, K. Zhang, X. Yu and K. Chang, *ACS Catal.*, 2021, **11**, 11429–11439.
46 H. Sun, W. Zhang, J.-G. Li, Z. Li, X. Ao, K.-H. Xue, K. K. Ostrikov, J. Tang and C. Wang, *Appl. Catal., B*, 2021, **284**, 119740.
47 S. Liu, H. Zhang, E. Hu, T. Zhu, C. Zhou, Y. Huang, M. Ling, X. Gao and Z. Lin, *J. Mater. Chem. A*, 2021, **9**, 23697–23702.
48 T. Han, Y. Wei, X. Jin, H. Jiu, L. Zhang, Y. Sun, J. Tian, R. Shang, D. Hang and R. Zhao, *J. Mater. Sci.*, 2019, **54**, 7119–7130.
49 L. Geng, P. Zhu, Y. Wei, R. Guo, C. Xiang, C. Cui and Y. Li, *Cellulose*, 2019, **26**, 2833–2847.
50 N. Cai, M. Chen, M. Liu, J. Wang, L. Shen, J. Wang, X. Feng and F. Yu, *J. Mol. Liq.*, 2019, **289**, 111060.
51 Q. Qin, T. Liu, J. Zhang, R. Wei, S. You and Y. Xu, *J. Hazard. Mater.*, 2021, **419**, 126447.
52 H. Trabelsi, M. Bejar, E. Dhahri, M. P. F. Graca, M. A. Valente, M. J. Soares and N. A. Sobolev, *Appl. Surf. Sci.*, 2017, **426**, 386–390.
53 C. Foo, Y. Li, K. Lebedev, T. Chen, S. Day, C. Tang and S. C. E. Tsang, *Nat. Commun.*, 2021, **12**, 661.